

Calibrating the terminations of Cryogenian global glaciations

Chuanming Zhou¹, Magdalena H. Huyskens², Xianguo Lang¹, Shuhai Xiao³,

Qing-Zhu Yin²

¹*CAS Key Laboratory of Economic Stratigraphy and Palaeogeography, Nanjing Institute of Geology and Palaeontology and Center for Excellence in Life and Palaeoenvironment, Chinese Academy of Sciences, Nanjing 210008, China*

²*Department of Earth and Planetary Sciences, University of California at Davis, CA 95616-8605, USA*

³*Department of Geosciences, Virginia Tech, Blacksburg, VA 24061, USA*

1. Cryogenian stratigraphy in South China

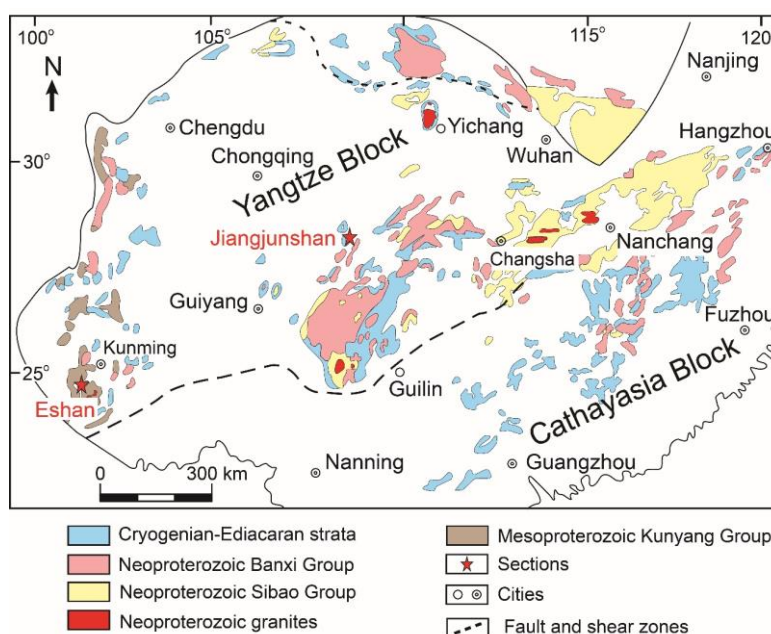


Figure DR1. The outcrops of the Precambrian strata in South China and locations of the Jiangjunshan and Eshan sections. Modified from (Wang and Li, 2003).

Cryogenian successions in the Yangtze block are highly variable in both stratigraphic thickness and completeness (Zhang et al., 2011). In the depocenter of the rift basin (e.g., the Sanjiang section bordering western Hunan, eastern Guizhou, and

northern Guangxi provinces), the Cryogenian succession is several thousand meters thick, consisting of the Chang'an (diamictite, ~ 1500 m), Fulu (ironstone and sandstone, ~ 600 m), Tiesi'ao (diamictite, ~ 20 m), Datangpo (manganiferous shale and siltstone, ~ 12 m), and Nantuo (diamictite, ~ 1100 m) formations. In the transitional/slope facies to the northwest of the depocenter, such as at the Yangjiaping section in northwestern Hunan Province and Jiangjunshan/Zhailanggou sections in eastern Guizhou Province, the Cryogenian succession is about one hundred to several hundred meters thick, and consists of Gucheng/Tiesi'ao Formation diamictite, interglacial Datangpo Formation black shale and siltstone, and the Nantuo Formation diamictite. The Xieshuihe Formation sandstone underlying the Gucheng Formation and the Liangjiehe Formation sandstone underlying the Tiesi'ao Formation in the transitional/slope facies are generally considered Tonian in age (Yin et al., 2003), although Zhang et al. (2011) and Lan et al. (2015) suggested them to be Cryogenian based on lithostratigraphic correlation. Further northwestward in the shallow-water platform facies, e.g., at the Jiulongwan section in the western Hubei Province and Eshan section in eastern Yunnan Province, only the <100-m-thick Nantuo Formation diamictite was deposited and preserved between the Tonian Liantuo/Chengjiang Formation (~ 720–780 Ma) sandstone and the basal Ediacaran cap dolostone/siliciclastic rocks. Thus, as a general pattern, Cryogenian successions are more complete and thicker in deep-water basinal facies to the southeast than in shallow-water platform facies to the northwest (Figure DR2).

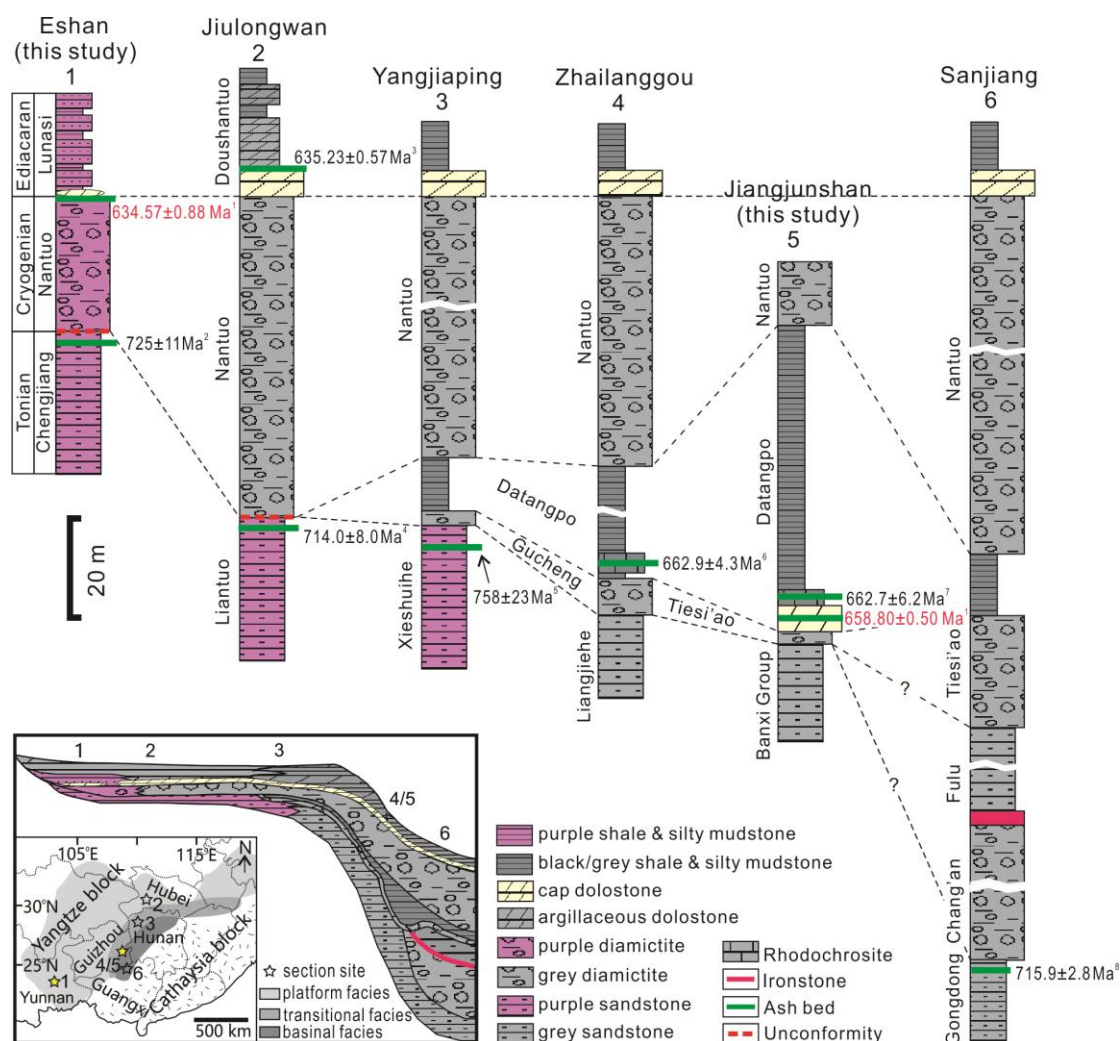


Figure DR2. Simplified paleogeography, lithostratigraphy and radiometric dates of Cryogenian successions in South China. Question marks refer to uncertainty on the correlation between the Tiesi'ao Formation in the transitional facies and Tiesi'ao+Fulu+Chang'an formations in the basinal facies. Data sources: 1, present study; 2, Cui et al., 2013; 3, Condon et al., 2005; 4, Lan et al., 2015; 5, Yin et al., 2003; 6, Zhou et al., 2004; 7, Yu et al., 2017; 8, Lan et al., 2014. Analytical methods: CA-ID-TIMS for 1 and 3; ID-TIMS for 6; SIMS for 4 and 8; SHRIMP for 2 and 5; LA-ICP-MS for 7.

2. Field photos of lithofacies and sampled horizons

2.1. Field photos of Jiangjunshan section



Figure DR3. Field photographs pertinent to sample 17LSJ-17. (A) Jiangjunshan section (28°9'34.56"N, 108°55'5.16"E) in eastern Guizhou Province, showing Cryogenian Tiesi'ao and Datangpo formations, and a dolomitic tuffaceous bed (arrow; sample 17LSJ-17) within the cap dolostone at the base of Datangpo Formation. Person for scale is 175 cm. (B) Close-up view of the dolomitic tuffaceous bed (arrow). Hammerhead to the lower right corner is 16 cm long. (C–D) Dolomitic diamictite of the Tiesi'ao Formation showing the occurrence of glaciogenic clasts (arrows).

2.2. Stratigraphy and field photos of Eshan and Tiechang section

At the Eshan section (24 °12'15.66"N, 102 °28'31.33"E) in eastern Yunnan Province of South China, the terminal Cryogenian Nantuo Formation unconformably overlies purple sandstone of the Tonian Chengjiang Formation and conformably underlies siliciclastic rocks of the Ediacaran Lunasi Formation (Figure DR4A-B). The Nantuo Formation at Eshan is ~ 25 m thick and consists mainly of purple diamictite (Figure DR4A, C). A ~ 20-cm-thick grey tuffaceous mudstone layer (sample ES-1) occurs at the top of the Nantuo Formation (Figure DR4D). The occurrence of pebble-sized dropstones (Figure DR4E-F) in this layer suggests input of ice-rafted clasts.

The cap dolostone unit, which occurs widely atop the Nantuo Formation diamictite in the Yangtze block of South China, is absent at the Eshan section and in many areas of western Yangtze block (eastern Yunnan and central Sichuan provinces). Instead, it is represented by discontinuous dolostone nodules in eastern Yunnan Province. At the Tiechang section (25 °05'30.00"N, 103 °25'22.92"E), a dolostone bed (up to 0.8 m thick), which marks the basal part of the Ediacaran Lunasi Formation, occurs between the underlying Nantuo Formation purple diamictite and the overlying purple siltstone. At the base of this dolostone bed, there occur glaciogenic clasts indicative of continuous deposition and hence conformable nature of the boundary between the diamictite and the overlying dolostone. The stratigraphic position and sedimentary features of this dolostone bed indicate that it represents the cap dolostone overlying the Nantuo Formation diamictite.

At the Eshan section, no sedimentary break was observed between the grey tuffaceous mudstone layer and the underlying diamictite. The occurrence of ice-rafted pebbles within the tuffaceous mudstone layer indicates its close stratigraphic relationship with the Nantuo Formation. Thus, the tuffaceous mudstone layer at Eshan is placed in the topmost Nantuo Formation.

At the Jiulongwan section, glaciogenic clasts also occur in the lower part of the cap dolostone (which is ~3.3 m thick), suggesting that the contact between the terminal Cryogenian Nantuo Formation diamictite and the basal Ediacaran Doushantuo cap dolostone is a conformable boundary. The 635.23 ± 0.57 Ma ash dated by Condon et al. (2005) occurs immediately above the cap dolostone.



Figure DR4. Field photographs pertinent to sample ES-1. (A–F) Eshan section (24°12'15.66"N, 102°28'31.33"E) in eastern Yunnan Province. (A) The boundary between purple diamictite of the Cryogenian Nantuo Formation and purple silty mudstone of the Ediacaran Lunasi Formation. (B) Purple silty mudstone and sandstone interbedded with mudstone of the lower Lunasi Formation. (C) Striated pebble from the Nantuo Formation diamictite. (D) Grey tuffaceous mudstone layer (sample ES-1) at the topmost of the Nantuo Formation. (E–F)

Close-up views of the tuffaceous mudstone bed, showing glaciogenic dropstones (arrow). (G–H) Tiechang section (25°05'30.00"N, 103°25'22.92"E) in eastern Yunnan Province. (G) Cap dolostone above the purple diamictite of the Nantuo Formation. (H) Close-up view of the lower part of the cap dolostone in (G), showing glaciogenic clasts within the cap dolostone (arrows). Geological hammer is ~ 30 cm long.

3. Analytical methods and results

Zircons were separated and concentrated from ~11 and ~10 kilograms of tuffaceous rock samples of 17LSJ-17 and ES-1, respectively, by standard techniques at Yuneng Geological Service at Langfang in Hebei Province, China.

About 200 zircon grains were recovered from sample 17LSJ-17, and 700 from sample ES-1. A subset of more than 100 randomly selected grains was annealed in quartz vials at 900 °C for 48 h in a furnace. Zircons were rinsed in ethanol and placed on double sided sticky tape for U-Pb laser ablation screening analyses. These were performed to identify any detrital or inherited components and to select the youngest population of zircons for the subsequent, time-consuming and labor intensive chemical abrasion isotope dilution thermal ionization mass spectrometry (CA-ID-TIMS) analysis.

The selected zircons were taken off the tape and placed individually in 3-ml PFA vials. Zircons were rinsed with acetone followed by a rinse in 3 M HNO₃ and individual zircons were loaded into separate microcapsules in ~3 µl of 3 M HNO₃ and ~100 µl of concentrated HF were added. An assembly of 15 microcapsules were placed in a Parr dissolution vessel containing 7 ml of concentrated HF and traces of HNO₃. Zircons were leached for 15 h at 190 °C (Huyskens et al., 2016). The remaining zircons were transferred into 3-ml PFA vials and rinsed with MilliQ water, then treated with 6 M HCl onto a hotplate. Subsequently, the zircons were washed in multiple steps of MilliQ and 3 M HNO₃. For dissolution at 220 °C, the zircons were

placed in individual capsules, and ~3 µl of 3 M HNO₃ and ~100 µl of concentrated HF were added as well as a ²⁰²Pb-²⁰⁵Pb-²³³U-²³⁶U tracer (Huyskens et al., 2016). The samples were dried down and redissolved in 6 M HCl over-night, and subsequently evaporated to dryness. Samples were redissolved in 2.5 M HCl and Pb and U were separated from the matrix elements by standard HCl ion exchange chemistry (Krogh, 1973). The Pb fraction was dried down with 0.05 ml of 0.02 M H₃PO₄ and loaded onto zone refined Re filaments with a silica gel activator (Huyskens et al., 2012). Pb isotopic measurements were performed on a *Triton Plus* TIMS at UC Davis. The *Triton plus* TIMS is equipped with nine faraday cups and one secondary electron multiplier and has a total of ten amplifiers, six of which are equipped with 10¹³ Ω resistors and four with 10¹¹ Ω resistors. Those can be connected to any of the faraday cups through a relay matrix. Gain calibration procedure of the amplifiers followed the procedure described in Trinquier (2016). In short, we used the La Jolla Nd isotopic standard (Lugmair and Carlson, 1978) for gain calibration of the amplifiers with 10¹³ Ω resistors. Two amplifiers with 10¹¹ Ω resistors were calibrated with the built-in calibration board of the instrument and coupled to the faraday cups measuring ¹⁴⁶Nd and ¹⁴⁴Nd. All other Nd isotopes were measured on Faraday cups coupled with amplifiers equipped with 10¹³ Ω resistors. The ¹⁴⁶Nd/¹⁴⁴Nd ratio was used for fractionation correction and the measured ^{14x}Nd/¹⁴⁴Nd ratio was used to determine the relative gain for the amplifiers with 10¹³ Ω resistors. This procedure was repeated to calibrate all six 10¹³ Ω amplifiers. Subsequently, a yield calibration for the SEM was performed at the beginning of the day using the Pb standard SRM 981. The accuracy of the calibration was checked using this standard daily. Due to difference in response times of the various detectors the ion beam intensity was kept close to constant in all measurements and the idle time was set to 10 seconds (Klaver et al., 2016; von Quadt

et al., 2016). Most samples were measured in static mode with ^{204}Pb in the axial SEM, while all other isotopes were collected in Faraday cups coupled with $10^{13} \Omega$ resistor amplifier boards. Samples with very low Pb content were measured on the SEM in peak jumping mode.

U isotope dilution measurements were performed on a *Neptune Plus* at UC Davis. The samples were introduced with an ESI APEX introduction system using a 50 $\mu\text{l}/\text{min}$ nebulizer. During these measurements, the Neptune was equipped with an X skimmer cone and Jet sample cone. Prior to each analytical session, a gain calibration of the amplifiers and a long baseline measurement were performed. Faraday cups measuring ^{238}U and ^{235}U were coupled with $10^{12} \Omega$ resistors and ^{233}U and ^{236}U were coupled with $10^{11} \Omega$ resistors. Data were collected for 30 cycles with 8 s integration time per cycle and corrected for instrumental mass dependent fractionation using an exponential law based on the known ^{233}U - ^{236}U ratio of IRMM-3636 (Verbruggen et al., 2008). Samples were bracketed with the Uranium isotopic standard CRM 112a. The $^{238}\text{U}/^{236}\text{U}$ ratio of the samples was additionally corrected using the known $^{238}\text{U}/^{235}\text{U}$ ratio of CRM 112a of 137.837 (Richter et al., 2010) using a linear correction. Total procedural blanks for U is 0.1 pg.

U–Pb ages and uncertainties were calculated using the algorithms of Schmitz and Schoene (2007), with the decay constants proposed by Jaffey et al. (1971) (Villa et al., 2016) and a $^{238}\text{U}/^{235}\text{U}$ ratio of 137.818 (Hiess et al., 2012). All non-radiogenic Pb was attributed to laboratory contamination. Weighted averages and concordia diagrams were produced using Isoplot (Ludwig, 2012).

The synthetic standard solution from the EARTHTIME project of 500 Ma, yielded a ^{206}Pb - ^{238}U date of $499.77 \pm 0.23 \text{ Ma}$ ($n=5$). For this standard, Pb and U were separated in the same way as the samples and measured with the same procedures.

The zircon grains from sample ES-1 show various coloring and are rounded, however, prismatic grains are present in this sample as well (Figure DR5). The laser ablation ICP-MS analyses confirmed that ES-1 has a detrital zircon component, which ranged in age from ~2.1 Ga to ~800 Ma (Figure DR6). Only ~25% of the analyzed grains are within the youngest population (<700 Ma). From this youngest group, seven grains were analyzed. One of those had very low radiogenic Pb content and is excluded (SB5-7). The remaining six grains show some scatter beyond analytical uncertainty (MSWD = 9) and range in $^{206}\text{Pb}/^{238}\text{U}$ age from 633.14 ± 0.87 Ma to 636.30 ± 0.59 Ma. This scatter can be caused by multiple factors, including the presence of inherited cores, antecrysts or xenocrysts or Pb loss. The age of the oldest of these grains is only agreeing within uncertainty with one other analysis (SB1-9) and is interpreted to be either of detrital origin or contain a xenocrystic core. The remaining five grains yield a $^{206}\text{Pb}/^{238}\text{U}$ date of 634.3 ± 1.0 Ma (95% confidence), with a slight overdispersion (MSWD = 3). For the best age estimate, we chose the most consistent group of four grains, excluding the youngest grain due to potential Pb loss. The group of four grains yield a $^{206}\text{Pb}/^{238}\text{U}$ age of $634.57 \pm 0.88/0.90/1.61$ Ma (MSWD = 1.4, 95% confidence, Fig. 2 and Figure DR7). Three levels of uncertainty are reported, respectively representing analytical uncertainty only/analytical and tracer uncertainties/analytical and tracer and decay constant uncertainties (Villa et al., 2016). The same selected grains yield a concordia age of $634.92 \pm 0.51/0.61/1.48$ Ma.

The zircon grains from sample 17LSJ-17 show various coloring and some are rounded (Figure DR5). LA ICP-MS analyses revealed a minor detrital component of zircons ranging in age from ~2.1 Ga to ~750 Ma (Figure DR6). From the youngest (<700 Ma) group eleven single zircon grains were analyzed by CA-ID-TIMS. Out of those, one grain is discordant (SB5-1) and one is significantly older (SB5-5), which is

interpreted to represent a detrital grain. The remaining nine grains overlap within error and yield a $^{206}\text{Pb}/^{238}\text{U}$ age of $658.80 \pm 0.50/0.54/1.49$ Ma (MSWD = 1.4, 95% confidence). The same analyses yield a concordia age of $658.85 \pm 0.27/0.34/1.41$ Ma.

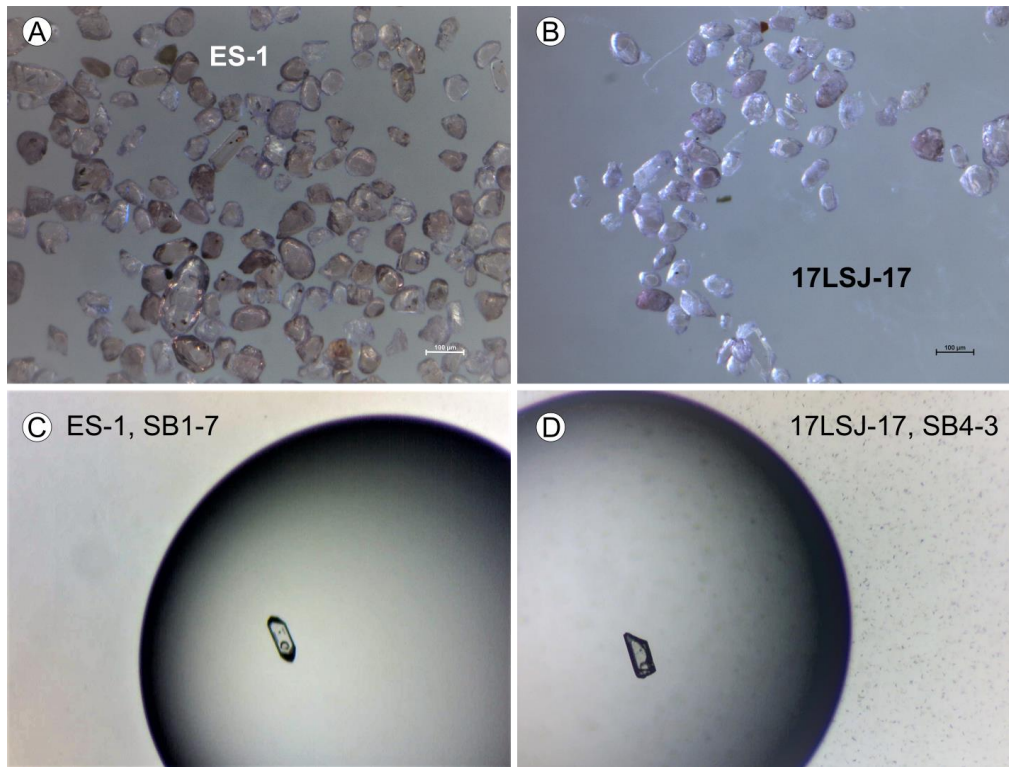


Figure DR5. Pictures (A) and (B) show the zircon separates of the samples ES-1 and 17LSJ-17, respectively. Both pictures are those of untreated samples. Pictures (C) and (D) show a single grain after leaching procedure for each sample that was analyzed by CA-ID-TIMS. The zircon grains are inside a drop of 3 M HNO_3 . In both panel (C) and (D), a laser ablation pit from the screening analysis is visible. Both grains are ~ 120 μm long.

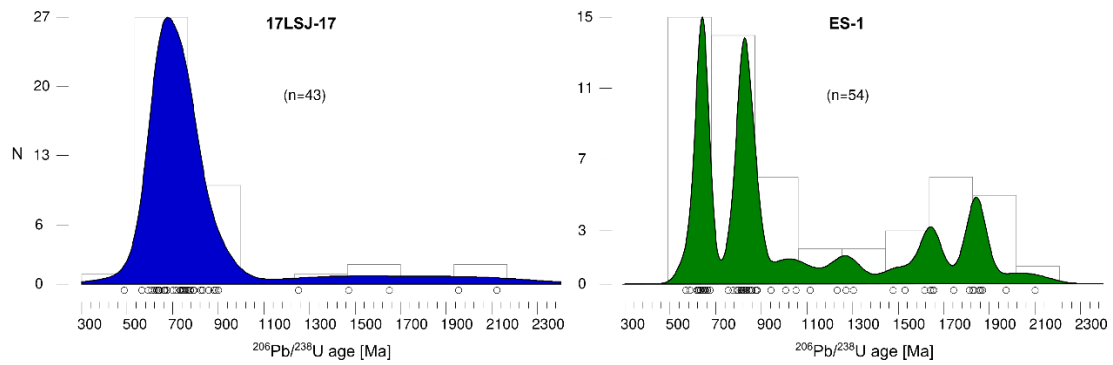


Figure DR6. Kernel density estimation (Vermeesch, 2012) and histogram of zircons analyzed by Laser ablation ICP-MS for samples 17 LSJ-17 and ES-1. All analyzed zircons are included, regardless of concordance. A high number ($>50\%$) of discordant grains is caused by both Pb loss and incorporation of common Pb on the surface of unpolished grains and these results were used as a guide to select the youngest grains for ID-TIMS.

Table DR1: U-Pb isotopic data of analyzed single zircon grains.

| Sample | analysis ID | Compositional Parameters | | | | Radiogenic Isotope Ratios | | | | | | | | Isotopic Ages | | | | | |
|-----------------|--------------|--------------------------|-----------------|-----------------|--------------------------------------|--------------------------------------|--------------------------------------|-------------|-------------------------------------|-------------|-------------------------------------|-------------|-------------|--------------------------------------|------------|-------------------------------------|-------------|-------------------------------------|-------------|
| | | Th | Pb* | Pb _c | ²⁰⁶ Pb/ ²⁰⁴ Pb | ²⁰⁸ Pb/ ²⁰⁶ Pb | ²⁰⁷ Pb/ ²⁰⁶ Pb | % err | ²⁰⁷ Pb/ ²³⁵ U | % err | ²⁰⁶ Pb/ ²³⁸ U | % err | corr. coef. | ²⁰⁷ Pb/ ²⁰⁶ Pb | ± | ²⁰⁷ Pb/ ²³⁵ U | ± | ²⁰⁶ Pb/ ²³⁸ U | ± |
| | | U | Pb _c | (pg) | (c) | (d) | (d) | (e) | (d) | (e) | (d) | (e) | | (f) | (e) | (f) | (e) | (f) | (e) |
| <u>17LSJ-17</u> | SB4-3 | 1.17 | 10.0 | 1.47 | 540 | 0.3621 | 0.06164 | 0.83 | 0.9143 | 0.90 | 0.1076 | 0.10 | 0.69 | 661 | 18 | 659.3 | 4.4 | 658.93 | 0.63 |
| | SB4-4 | 1.03 | 0.9 | 5.01 | 66 | 0.3269 | 0.06371 | 5.79 | 0.9466 | 6.16 | 0.1078 | 0.49 | 0.78 | 731 | 123 | 676.3 | 30.4 | 660.04 | 3.10 |
| | SB4-6 | 0.94 | 2.6 | 3.01 | 162 | 0.2931 | 0.06162 | 2.56 | 0.9141 | 2.74 | 0.1076 | 0.22 | 0.80 | 660 | 55 | 659.2 | 13.3 | 658.98 | 1.37 |
| | SB4-7 | 1.06 | 4.7 | 1.31 | 272 | 0.3285 | 0.06185 | 1.81 | 0.9164 | 1.95 | 0.1075 | 0.19 | 0.74 | 668 | 39 | 660.4 | 9.5 | 658.21 | 1.19 |
| | SB4-8 | 0.95 | 5.2 | 1.69 | 301 | 0.2955 | 0.06142 | 1.45 | 0.9118 | 1.56 | 0.1077 | 0.15 | 0.75 | 653 | 31 | 658.0 | 7.5 | 659.49 | 0.93 |
| | SB4-9 | 1.66 | 1.2 | 2.45 | 73 | 0.5096 | 0.06090 | 7.65 | 0.9045 | 8.07 | 0.1078 | 0.60 | 0.71 | 635 | 165 | 654.1 | 38.9 | 659.80 | 3.77 |
| | <i>SB5-1</i> | <i>1.2</i> | <i>1.2</i> | <i>2.2</i> | <i>81.2</i> | <i>0.3281</i> | <i>0.05277</i> | <i>7.92</i> | <i>0.7635</i> | <i>8.32</i> | <i>0.1050</i> | <i>0.55</i> | <i>0.73</i> | <i>318</i> | <i>180</i> | <i>576.0</i> | <i>36.6</i> | <i>643.46</i> | <i>3.39</i> |
| | SB5-2 | 1.3 | 10.3 | 1.0 | 544.8 | 0.3881 | 0.06152 | 0.97 | 0.9121 | 1.05 | 0.1076 | 0.11 | 0.76 | 656 | 21 | 658.2 | 5.1 | 658.68 | 0.71 |
| | SB5-3 | 1.2 | 2.3 | 1.4 | 138.2 | 0.3591 | 0.05963 | 3.83 | 0.8807 | 4.10 | 0.1072 | 0.37 | 0.75 | 589 | 83 | 641.3 | 19.5 | 656.27 | 2.30 |
| | SB5-4 | 1.1 | 1.8 | 4.2 | 114.0 | 0.3278 | 0.05965 | 4.78 | 0.8821 | 5.10 | 0.1073 | 0.40 | 0.81 | 590 | 104 | 642.1 | 24.3 | 657.06 | 2.50 |
| | <i>SB5-5</i> | <i>0.6</i> | <i>0.8</i> | <i>2.2</i> | <i>67.2</i> | <i>0.1673</i> | <i>0.06139</i> | <i>8.69</i> | <i>1.1207</i> | <i>9.22</i> | <i>0.1325</i> | <i>0.80</i> | <i>0.69</i> | <i>652</i> | <i>186</i> | <i>763.3</i> | <i>49.5</i> | <i>801.88</i> | <i>6.05</i> |
| <u>ES-1</u> | SB1-6 | 0.40 | 5.79 | 1.03 | 381.89 | 0.1242 | 0.06022 | 1.41 | 0.8584 | 1.56 | 0.1034 | 0.17 | 0.87 | 610 | 30 | 629.3 | 7.3 | 634.53 | 1.03 |
| | SB1-7 | 0.53 | 10.45 | 1.33 | 652.30 | 0.1636 | 0.06065 | 0.84 | 0.8649 | 0.93 | 0.1035 | 0.11 | 0.81 | 626 | 18 | 632.8 | 4.4 | 634.75 | 0.64 |
| | <i>SB1-9</i> | <i>0.49</i> | <i>12.81</i> | <i>0.65</i> | <i>803.69</i> | <i>0.1508</i> | <i>0.06102</i> | <i>0.84</i> | <i>0.8724</i> | <i>0.92</i> | <i>0.1037</i> | <i>0.10</i> | <i>0.92</i> | <i>639</i> | <i>18</i> | <i>636.9</i> | <i>4.4</i> | <i>636.30</i> | <i>0.59</i> |
| | SB1-8 | 0.63 | 4.36 | 0.82 | 275.90 | 0.1957 | 0.06105 | 2.25 | 0.8716 | 2.47 | 0.1036 | 0.26 | 0.90 | 640 | 48 | 636.4 | 11.7 | 635.44 | 1.55 |
| | <i>SB5-6</i> | <i>0.33</i> | <i>0.99</i> | <i>1.65</i> | <i>81.77</i> | <i>0.0998</i> | <i>0.05907</i> | <i>7.53</i> | <i>0.8300</i> | <i>8.00</i> | <i>0.1020</i> | <i>0.64</i> | <i>0.75</i> | <i>569</i> | <i>164</i> | <i>613.6</i> | <i>36.9</i> | <i>625.83</i> | <i>3.82</i> |
| | SB5-7 | 0.42 | 4.24 | 1.36 | 283.17 | 0.1305 | 0.06077 | 1.77 | 0.8651 | 1.91 | 0.1033 | 0.19 | 0.77 | 630 | 38 | 632.9 | 9.0 | 633.66 | 1.12 |
| | <i>SB5-8</i> | <i>0.53</i> | <i>9.81</i> | <i>0.64</i> | <i>612.55</i> | <i>0.1649</i> | <i>0.06087</i> | <i>1.23</i> | <i>0.8657</i> | <i>1.34</i> | <i>0.1032</i> | <i>0.14</i> | <i>0.82</i> | <i>634</i> | <i>26</i> | <i>633.2</i> | <i>6.3</i> | <i>633.14</i> | <i>0.87</i> |

analyses in italics are excluded from the weighted average calculation

(a) Model Th/U ratio calculated from radiogenic ²⁰⁸Pb/²⁰⁶Pb ratio and ²⁰⁷Pb/²³⁵U age.

(b) Pb* and Pb_c represent radiogenic and common Pb, respectively

(c) Measured ratio corrected for spike and fractionation only.

(d) Corrected for fractionation, spike, and common Pb; all common Pb was assumed to be blank with the isotopic composition of ²⁰⁶Pb/²⁰⁴Pb = 18.59 ± 0.65%; ²⁰⁷Pb/²⁰⁴Pb = 15.79 ± 0.70%; ²⁰⁸Pb/²⁰⁴Pb = 38.54 ± 0.65% (1σ).

(e) Errors are 2-sigma, propagated using the algorithms of Schmitz and Schoene (2007) and Crowley et al. (2007).

(f) Calculations are based on the decay constants of Jaffey et al. (1971) and a ²³⁸U/²³⁵U ratio of 137.818 (Hiess et al. 2012).

4. Review of high-precision U-Pb dates of the Marinoan deglaciation

The termination of the Marinoan glaciation is currently constrained by four high-precision U-Pb dates from three different continents (Fig. 3). Two of those samples are located within glaciogenic diamictites in Southern Australia (Cottons Breccia) and Namibia (Navachab Formation) and thus represent maximum age constraints for the termination of the glaciation. One age constraint is from directly atop the diamictite (Nantuo Formation, this study) and one on top of the cap dolostone (Doushantuo Formation) in South China, which are considered maximum and minimum age constraints respectively, for the termination of the Marinoan glaciation. The sample from the uppermost Cottons Breccia in King Island, Tasmania, shows a bimodal $^{206}\text{Pb}/^{238}\text{U}$ age distribution, with the dominant age group ~ 636 Ma and a minor peak at ~ 662 Ma based on SHRIMP results (Calver et al., 2013). The youngest age group was selected for CA-ID-TIMS measurements and resulted in an age of 636.41 ± 0.45 Ma (Calver et al., 2013). A second age constraint from near the end of the Marinoan glaciation is from within the diamictite of the Navachab Formation in Namibia. Within the volcanic ash bed Mesoproterozoic xenocrysts are present (Hoffmann et al., 2004) and within the younger group (< 640 Ma) the zircon ages show some dispersion (Figure DR7; Prave et al., 2016). The youngest group of five zircon grains yielded an age of 635.21 ± 0.59 Ma (Prave et al., 2016) and was interpreted to most closely represent the age of the volcanic eruption for the volcanic ash layer and its deposition.

For stratigraphic sections in South China, one tuffaceous mudstone (ES-1, this study) is located in the topmost Nantuo Formation, representing a maximum age constraint for the termination of the glaciation, and a volcanic ash layer in the Doushantuo Formation, on top of the cap dolostone (Condon et al., 2005), representing a minimum age constraint. Both of these samples contain detrital zircons and yield the same age within uncertainty. The zircons from sample ES-1 at the top of the Nantuo Formation show a $^{206}\text{Pb}/^{238}\text{U}$ age of 634.57 ± 0.88 Ma (this study) and a Concordia date of 635.23 ± 0.57 Ma was obtained for zircons from the volcanic ash

layer at the top of the cap dolostone (Condon et al., 2005). For the latter study, many zircons show signs of Pb loss and fall on a discordia line. For the reported age however, only three concordant grains out of twelve non-detrital zircons were used (Figure DR7).

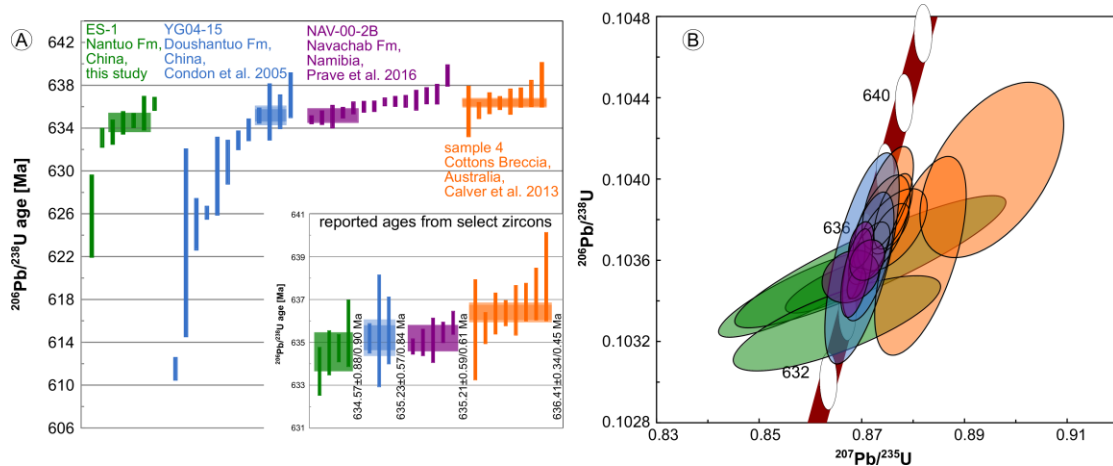


Figure DR7. Comparison of all high-precision U-Pb CA-ID-TIMS zircon data relevant to the Marinoan deglaciation. Panel (A) shows all individual zircon analyses except those that are detrital in origin. The light shaded bar across the individual analyses denotes the date and uncertainty for the selected zircons. The still lighter colored bar around it includes the tracer calibration uncertainty, which are insignificant for some data sets, due to the small increase in uncertainty. The insert shows only the zircon grains selected for date calculation and reported dates with internal uncertainty only (shaded bars) and tracer uncertainty (lighter shaded bars). Panel (B) shows the same selected grains in a concordia diagram.

References

- Calver, C. R., Crowley, J. L., Wingate, M. T. D., Evans, D. A. D., Raub, T. D., and Schmitz, M. D., 2013, Globally synchronous Marinoan deglaciation indicated by U-Pb geochronology of the Cottons Breccia, Tasmania, Australia: *Geology*, v. 41, p. 1127-1130.
- Condon, D., Zhu, M., Bowring, S., Wang, W., Yang, A., and Jin, Y., 2005, U-Pb ages from the neoproterozoic Doushantuo Formation, China: *Science*, v. 308, p. 95-98.
- Cui, X., Jiang, X., Wang, J., Zhuo, J., Xiong, G., Lu, J., Deng, Q., Wu, H., and Liu, J., 2013, Zircon U-Pb geochronology for the stratotype section of the Neoproterozoic Chengjiang Formation in central Yunnan and its geological significance: *Geoscience*, v. 27, p. 547-556.
- Hiess, J., Condon, D. J., McLean, N., and Noble, S. R., 2012, $^{238}\text{U}/^{235}\text{U}$ Systematics in Terrestrial Uranium-Bearing Minerals: *Science*, v. 335, p. 1610-1614.
- Hoffmann, K. H., Condon, D. J., Bowring, S. A., and Crowley, J. L., 2004, U-Pb zircon date from the Neoproterozoic Ghaub Formation, Namibia: Constraints on Marinoan glaciation: *Geology*, v. 32, p. 817.

- Huyskens, M. H., Iizuka, T., and Amelin, Y., 2012, Evaluation of colloidal silicagels for lead isotopic measurements using thermal ionisation mass spectrometry: *Journal of Analytical Atomic Spectrometry*, v. 27, p. 1439-1446.
- Huyskens, M. H., Zink, S., and Amelin, Y., 2016, Evaluation of temperature-time conditions for the chemical abrasion treatment of single zircons for U–Pb geochronology: *Chemical Geology*, v. 438, p. 25-35.
- Jaffey, A. H., Flynn, K. F., Glendeni, Le, Bentley, W. C., and Essling, A. M., 1971, Precision Measurement of Half-Lives and Specific Activities of ^{235}U and ^{238}U : *Physical Review C*, v. 4, p. 1889-1906.
- Klaver, M., Smeets, R. J., Koornneef, J. M., Davies, G. R., and Vroon, P. Z., 2016, Pb isotope analysis of ng size samples by TIMS equipped with a $10^{13}\Omega$ resistor using a ^{207}Pb – ^{204}Pb double spike: *Journal of Analytical Atomic Spectrometry*, v. 31, p. 171-178.
- Krogh, T., 1973, A low-contamination method for hydrothermal decomposition of zircon and extraction of U and Pb for isotopic age determinations: *Geochimica Et Cosmochimica Acta*, v. 37, p. 485-494.
- Lan, Z., Li, X.-H., Zhang, Q., and Li, Q.-L., 2015, Global synchronous initiation of the 2nd episode of Sturtian glaciation: SIMS zircon U–Pb and O isotope evidence from the Jiangkou Group, South China: *Precambrian Research*, v. 267, p. 28-38.
- Lan, Z., Li, X., Zhu, M., Chen, Z.-Q., Zhang, Q., Li, Q., Lu, D., Liu, Y., and Tang, G., 2014, A rapid and synchronous initiation of the wide spread Cryogenian glaciations: *Precambrian Research*, v. 255, p. 401-411.
- Ludwig, K., 2012, Isoplot 3.75. A Geochronological toolkit for Microsoft Excel. Berkeley Geochronology Center, Spec. Pub. 5.
- Lugmair, G., and Carlson, R., The Sm-Nd history of KREEP, *in* *Proceedings Lunar and Planetary Science Conference Proceedings 1978, Volume 9*, p. 689-704.
- Prave, A. R., Condon, D. J., Hoffmann, K. H., Tapster, S., and Fallick, A. E., 2016, Duration and nature of the end-Cryogenian (Marinoan) glaciation: *Geology*, v. 44, p. 631-634.
- Richter, S., Eykens, R., K ühn, H., Aregbe, Y., Verbruggen, A., and Weyer, S., 2010, New average values for the $n(238\text{U})/n(235\text{U})$ isotope ratios of natural uranium standards: *International Journal of Mass Spectrometry*, v. 295, p. 94-97.
- Schmitz, M. D., and Schoene, B., 2007, Derivation of isotope ratios, errors, and error correlations for U-Pb geochronology using ^{205}Pb – ^{235}U –(^{233}U)-spiked isotope dilution thermal ionization mass spectrometric data: *Geochemistry Geophysics Geosystems*, v. 8, Q08006.
- Trinquier, A., 2016, Fractionation of Oxygen Isotopes by Thermal Ionization Mass Spectrometry Inferred from Simultaneous Measurement of $^{17}\text{O}/^{16}\text{O}$ and $^{18}\text{O}/^{16}\text{O}$ Ratios and Implications for the ^{182}Hf – ^{182}W Systematics: *Analytical Chemistry*, v. 88, p. 5600-5604.
- Verbruggen, A., Alonso, A., Eykens, R., Kehoe, F., K ühn, H., Richter, S., and Aregbe, Y., 2008, Preparation and Certification of IRMM-3636, IRMM-3636a and IRMM-3636b: OPOCE, 24pp.
- Vermeesch, P., 2012. On the visualisation of detrital age distributions. *Chemical Geology*, 312-313: 190-194.
- Villa, I. M., Bonardi, M. L., De Bi èvre, P., Holden, N. E., and Renne, P. R., 2016, IUPAC-IUGS status report on the half-lives of ^{238}U , ^{235}U and ^{234}U : *Geochimica et Cosmochimica Acta*, v. 172, p. 387-392.

- von Quadt, A., Wotzlaw, J.-F., Buret, Y., Large, S. J. E., Peytcheva, I., and Trinquier, A., 2016, High-precision zircon U/Pb geochronology by ID-TIMS using new 10^{13} ohm resistors: *Journal of Analytical Atomic Spectrometry*, v. 31, p. 658-665.
- Wang, J., and Li, Z.-X., 2003, History of Neoproterozoic rift basins in South China: implications for Rodinia break-up: *Precambrian Research*, v. 122, p. 141-158.
- Yin, C., Liu, D., Gao, L., Wang, Z., Xing, Y., Jian, P., and Shi, Y., 2003, Lower boundary age of the Nanhua System and the Gucheng glacial stage: Evidence from SHRIMP II dating: *Chinese Science Bulletin*, v. 48, p. 1657-1662.
- Yu, W., Algeo, T. J., Du, Y., Zhou, Q., Wang, P., Xu, Y., Yuan, L., and Pan, W., 2017, Newly discovered Sturtian cap carbonate in the Nanhua Basin, South China: *Precambrian Research*, v. 293, p. 112-130.
- Zhang, Q., Chu, X., and Feng, L., 2011, Neoproterozoic glacial records in the Yangtze Region, China, *in* Arnaud, E., Halverson, G. P., and Shields-Zhou, G., eds., *The Geological Record of Neoproterozoic Glaciations*, Volume 36, Geological Society, London, *Memoirs*, p. 357-366.
- Zhou, C., Tucker, R., Xiao, S., Peng, Z., Yuan, X., and Chen, Z., 2004, New constraints on the ages of Neoproterozoic glaciations in South China: *Geology*, v. 32, p. 437-440.